Enhancing In-vitro Stability of Albumin Microbubbles Produced Using Microfluidic T-junction Device

Aaqib H. Khan[#], Swarupkumar Surwase[#], Xinyue Jiang†, Mohan Edirisinghe†, and Sameer V. Dalvi[#]*

Chemical Engineering, Indian Institute of Technology Gandhinagar, Palaj, Gandhinagar - 382355, Gujarat, India

†Department of Mechanical Engineering, University College London (UCL), London WC1E 7JE, U.K.

Abstract: Microfluidics is an efficient technique for continuous synthesis of monodispersed microbubbles. However, microbubbles produced using microfluidic devices possess lower stability due to quick dissolution of core gas when exposed to an aqueous environment. This work aims at generating highly stable monodispersed albumin microbubbles using microfluidic T-junction devices. Microbubble generation was facilitated by an aqueous phase consisting of Bovine serum albumin (BSA) as a model protein, and nitrogen (N_2) gas. Microbubbles were chemically crosslinked using dilute glutaraldehyde (0.75 % v/v) solution, and thermally crosslinked by collecting microbubbles in hot water maintained at 368 (± 2) K. These microbubbles were then subjected to in-vitro dissolution in an air-saturated water. Microbubbles crosslinked with a combined treatment of thermal and chemical crosslinking (TC & CC) had longer dissolution time compared to microbubbles chemically crosslinked (CC) alone, thermally crosslinked (TC) alone and non-crosslinked microbubbles. Circular Dichroism (CD) spectroscopy analysis revealed that % reduction in alpha-helices of BSA was higher for the combined treatment of TC & CC when compared to other treatments. In contrast to non-crosslinked microbubbles where microbubble shell dissolved completely, a significant shell detachment was observed during the final phase of the dissolution for crosslinked microbubbles captured using high speed camera, depending upon the extent of crosslinking of the microbubble shell. SEM micrographs of the microbubble shell revealed the shell thickness of microbubbles treated with TC & CC to be highest compared to only thermally or only chemically crosslinked microbubbles. Comparison of microbubble dissolution data to a mass transfer model showed that shell resistance to gas permeation was highest for microbubbles subjected to a combined treatment of TC & CC.

Keywords: Microbubbles; microfluidics; crosslinking; dissolution

Corresponding Author

***E-mail: sameervd@iitgn.ac.in; Phone: 091-79-2395 2408**

1. Introduction: Microbubbles are micron sized gas bubbles stabilized by shell materials such as proteins[1, 2], lipids[3], and polymers and suspended in aqueous medium. Microbubbles are extensively used in the biomedical field for targeted drug or gene delivery[4] and ultrasound contrast imaging[5-7]. Commonly used microbubble formation techniques include sonication[2, 8], electro-hydrodynamic atomization[9, 10], microfluidic devices[11, 12] , gyration[13], amalgamation[14, 15], saline shaking[16] and freeze drying[17]. Among all these reported methods, sonication, gyration and amalgamation produce large number of microbubbles within a small time interval. However, the microbubbles produced using these methods are always polydisperse[18]. Hence, additional steps in the form of size isolation are required to produce monodisperse microbubbles relevant for biomedical applications. In contrast to other microbubble synthesis techniques, microfluidics is one of the promising techniques that can extensively control the size of microbubbles and can continuously generate highly monodisperse microbubbles[19]. Depending on the flow geometries and contacting patterns of liquid and gaseous stream, microfluidic devices are classified as flow-focusing[20], co-flow focusing[21], and T-junction (cross-flow type) microfluidics[22, 23]. Irrespective of the microfluidic device, microbubbles are formed due to the gas-liquid interface instability where, the gaseous stream breaks periodically into small sized gas pockets and consequently gets encapsulated in aqueous solution of protein or lipid to form bubbles[24]. Interfacial forces significantly influence the microbubble formation using microfluidic devices. The effect of interfacial forces can be characterized by various dimensionless numbers, such as $Capillary\ no.\ (Ca) = \frac{\mu u}{\sigma}$ which is the ratio of viscous force and surface tension force, and $Weber\ no.\ (We) = \frac{\rho u^2 d}{\sigma}$ which is the ratio of inertia and surface tension force. There are many reports in the literature which study the effect of variation in these dimensionless numbers during operation of microfluidic devices on microbubble formation and microbubble size and size distribution.[25-27]

However, stability of these microbubbles is very poor when compared to microbubbles produced using sonication. The maximum stability reported for microbubbles produced using microfluidic devices such as T-junction is ~ 40 mins for BSA microbubbles with nitrogen gas core and average size of 260 ± 10 μm[11]. Therefore, this work was focused on increasing the *in vitro* dissolution stability of BSA microbubbles produced using microfluidics. BSA microbubbles produced using a T-junction were treated using thermal and chemical crosslinking treatment and their *in vitro* dissolution was captured using high-speed camera. The

radius v/s time data recorded for microbubble dissolution was numerically fit to a mass transfer model to estimate shell resistances using constrained optimization. Finally, the shell of microbubbles was characterised using FE-SEM and AFM, to measure the shell thickness and understand the surface morphology of the shell, respectively and correlate those with in-vitro dissolution times.

2. Methods and Materials

2.1 Materials: Bovine serum albumin (BSA) (purity >98%, as lyophilized powder) was obtained from Proliant Biologicals, New Zealand. Glutaraldehyde (GA, Grade 1, 25% in H_2O) was obtained from Sigma-Aldrich India. These were used without further purification. Nitrogen gas (Ultrahigh pure grade), used as a dispersed phase during microbubble preparation, was purchased from JP gas suppliers India.

2.2 Solution preparation: Aqueous phase for microbubble production was prepared by dissolving 15 % (w/w) BSA in deionized water at room temperature (~25 ℃) with constant magnetic stirring for 1 hr. Dilute glutaraldehyde solution (0.75 % (v/v)) was prepared by diluting GA (25% v/v) in DI water for chemical crosslinking.

2.3 Measurement of physicochemical properties of the solution: Physical properties of the solution such as viscosity, surface tension, and density were measured using standard calibrated equipment as follows (Table S1). Viscosity was measured by using Anton Paar, modular compact rheometer-302. Surface tension of the BSA solution was measured by the pendant drop method and density was measured using the gravimetric method. All these measurements were done at room temperature (~25℃).

2.4 Experimental setup

2.4.1 Microbubble production and characterization

The experimental setup consisted of a cross-flow type microfluidic T- junction which was custom made out of a Polydimethylsiloxane (PDMS) block of dimension (20 mm × 20 mm × 10 mm), and consisted of 1.6 mm hollow channels. Teflon Fluorinated Ethylene Polypropylene (TFEP) capillaries with outer diameter of 1.6 mm and with inner diameter 200 µm were inserted into the PDMS block. High-grade HPLC fittings were used to connect the tube to the PDMS block to avoid any leakage. A subsequent third capillary was placed into the block, perpendicularly oriented to other tubes to develop the cross-flow. Fig. 1 depicts the assembled schematic representation of the experimental setup. The top capillary of the T-junction was connected to a gas-regulator connected to the nitrogen gas tank. The inlet gas pressure was monitored using a digital pressure

gauge (EN-400, purchased from Adarsh Industries, Mumbai-India). An aqueous phase was injected into the T-junction by a syringe pump, Genie Touch™, to allow non-pulsating liquid flow. A high-speed camera (Photron FASTCAM Mini UX) was used to capture microbubbles formation in the T-junction. The videos were observed and recorded at constant frame rate of 4000 frames/sec. Microbubbles produced by T- junction were transferred over a glass slide and observed under an optical microscope (Nikon Eclipse Ni inverted microscope) with a 10X objective lens. Captured optical images of microbubbles were exported to an image processing software (Image J), to measure diameter of microbubbles. High-speed videos of microbubble formation were processed to estimate the production rate of the microbubble formation. The number of microbubbles pinched off in a recorded video was calculated as the bubble count. The production rate (bubble per sec) was calculated using equation 1.[28]

$$\text{Bubble production rate (bubbles per sec)} = \frac{\text{Bubbles count}}{\text{Total number of frames}} \times \frac{\text{Frames}}{\text{sec}} \quad (1)$$

2.4.2 Crosslinking of microbubbles

Crosslinking of freshly synthesized microbubbles was facilitated by thermal and chemical crosslinking. Hot DI water maintained at 368 ± 2 K was used as the aqueous medium for collection of freshly synthesized microbubble from microfluidic T-junction. Chemical crosslinking of the microbubbles was achieved by connecting two T-junction in series with 0.75 % (v/v) glutaraldehyde solution flowing through the 2nd T-junction. Dual crosslinking treatment, i.e. chemically as well as thermal crosslinking (CC & TC) was achieved by introducing 0.75 % (v/v) glutaraldehyde solution through the 2nd T-junction and collecting microbubbles in hot DI water maintained at 368 ± 2 K (95 ± 2 ℃).

2.5 Microbubble dissolution

A custom-made dissolution chamber (Fig. S1) made of acrylic was used to observe the *in-vitro* behaviour of single microbubble dissolution. The dissolution behaviour of microbubbles with a diameter of ~270 µm was observed under optical microscope (Nikon Eclipse Ni) at magnification of 10 X and 100 X and recorded until the complete dissolution of the microbubbles.

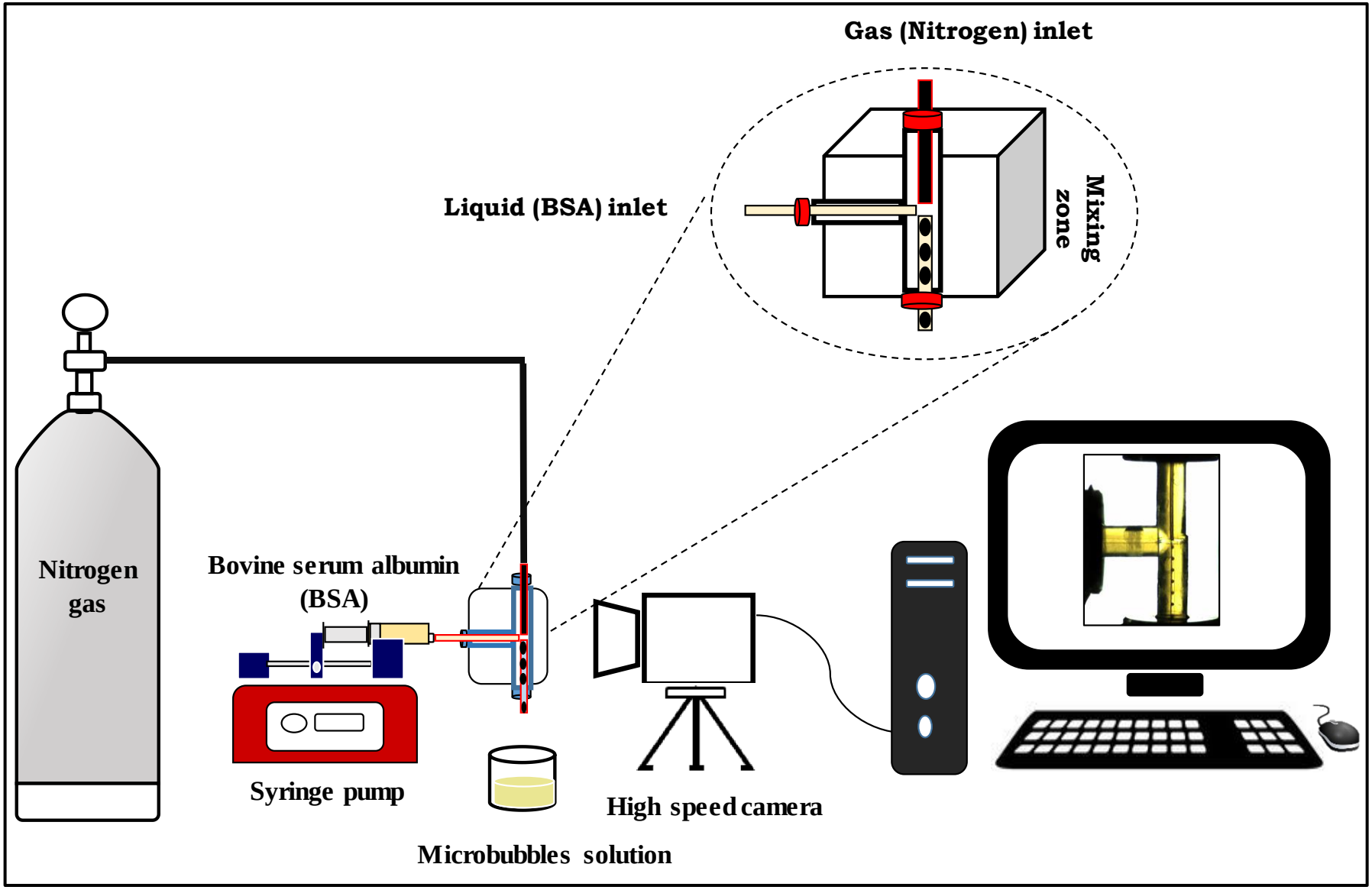

Figure 1: Schematic of experimental setup for microbubble generation with BSA as the aqueous solution, N_2 as the gaseous core in a single T-junction microfluidic device with no crosslinking treatment.

2.6 FE-SEM and AFM Imaging of Microbubble Shell

Microbubbles treated with different crosslinking formulations were collected over silicon wafer and Mica sheets for FE-SEM (JSM-7600F, JEOL) and AFM (Multimode 8, Bruker) analysis, respectively. Microbubbles were vacuum desiccated immediately after synthesis for 72 hours for drying. After drying, the BSA shells were platinum-coated for 100 secs and imaged using SEM, operating at 5 kV accelerating voltage, up to 25000X magnification. The surface topography of the microbubble shells was imaged by operating AFM in tapping mode.

3. Microbubble Dissolution Model

3.1 Model Equations

A two-way mass transfer dissolution model was used to understand the dissolution behaviour of Nitrogen (N_2) microbubbles in an air (comprising of N_2 & O_2) saturated aqueous environment. The dissolution model used in this work is similar to the two-way mass transfer models developed in earlier work[29, 30]. Fig. 2 presents the schematic of gas exchange phenomena occurring during dissolution of microbubbles in an air saturated environment. The gas in the core and the outer environment is assumed to be ideal gas.

Briefly, the model equations were derived as follows[29]

Mole balance of gas (A) over the microbubble gives,

$$N_A = \frac{-1}{A}\frac{dn_A}{dt}, A = 4\pi R^2 \quad (2)$$

N_A is the molar flux of A across the interface (mol/m^{2}s) and n_A is the number of moles of A in the microbubble core.

Molar flux of N_2 (A) in terms of overall mass transfer coefficient,

$$N_A = K_{l,A}\left(L_A C_{Ag} - f C_{Al,\infty}\right) \quad (3)$$

$K_{l,A}$ is the overall mass transfer coefficient, f is a degree of saturation of surrounding medium, and L_A is the Ostwald coefficient. Overall mas transfer resistance ($\frac{1}{K_{l,A}}$) is the sum of shell resistance, accounted by energy barrier model[31] $\Omega_{s,A} = \Omega_n \exp(\frac{\pi r_p^2(\sigma_0-\sigma)}{k_b T})$, and resistance offered by the liquid film $\frac{1}{k_L} = \frac{R}{D_{AL}}$. Therefore, the overall mass transfer resistance is given by $\frac{1}{K_{l,A}} = \Omega_{n,A}\exp(\frac{\pi r_p^2(\sigma_0-\sigma)}{k_b T}) + \frac{R}{D_{AL}}$.

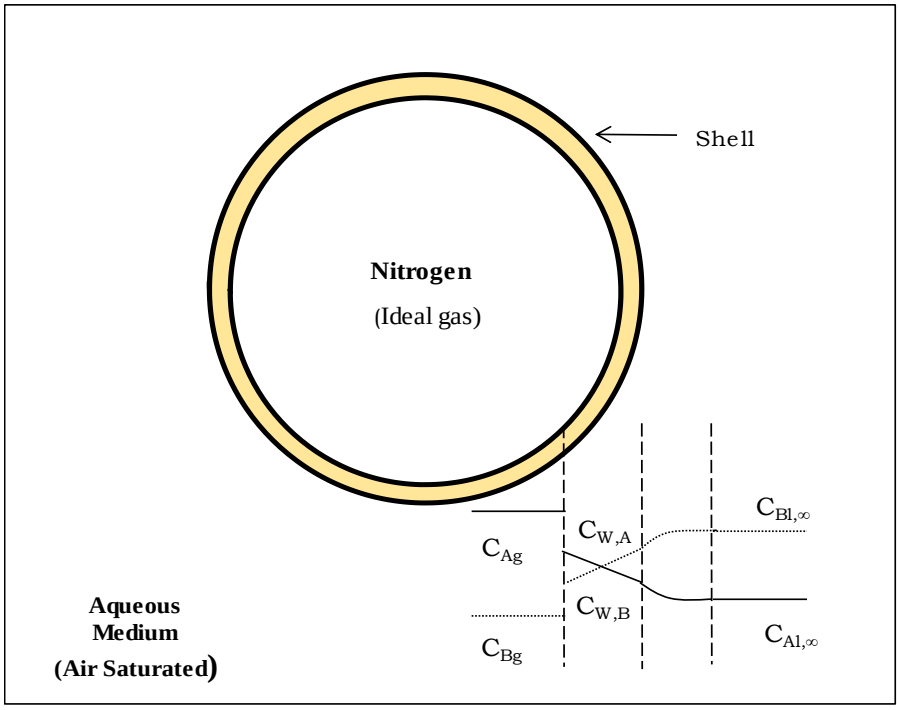

Figure 2: Schematic of concentration profiles of N_2 (A) and O_2 (B) during dissolution of N_2 microbubble in an air saturated environment

Combining equation 2 and 3 gives,

$$\frac{dn_A}{dt} = -4\pi R^2 K_{l,A}\left(L_A C_{Ag} - f C_{Al,\infty}\right),\ C_{Ag} = \frac{3n_A}{4\pi R^3} \tag{4}$$

Therefore, equation 4 becomes;

$$\frac{dn_A}{dt} = -4\pi R^2 K_{l,B}\left(\frac{3n_A L_A}{4\pi R^3} - f C_{Al,\infty}\right), \text{where } \frac{1}{K_{l,A}} = \Omega_{n,A}\exp\left(\frac{\pi r_{p1}^2(\sigma_0-\sigma)}{k_b T}\right) + \frac{R}{D_{AL}} \tag{5}$$

Similarly, molar flux for O_2 (B) can be given as;

$$\frac{dn_B}{dt} = -4\pi R^2 K_{l,B}\left(L_B\frac{3n_B}{4\pi R^3} - f C_{Bl,\infty}\right), \text{where } \frac{1}{K_{l,B}} = \Omega_{n,B}\exp\left(\frac{\pi r_{p2}^2(\sigma_0-\sigma)}{k_b T}\right) + \frac{R}{D_{BL}} \tag{6}$$

The pressure inside the bubble at any time (t) is given as;

$$P_g V = (n_A + n_B)RT, where\ P_g = P_{atm} + \frac{2\sigma}{R} \tag{7}$$

3.2 Computational methodology

The two-way mass transfer model described in Section 3.1 was solved with the help of a constrained single optimization function, Fmincon available in Matlab 2018. Equations (5,6) & (7) were used to estimate two unknown parameters; shell resistance (Ω_A) for the transfer of core gas N_2 (A) and shell resistance (Ω_B) for the

transfer of O_2 (B). The initial surface tension (σ_0) was assumed to be 36 mN/m and elasticity of shell (E_S) was assumed to 45 mN/m similar to a previous report on of albumin shelled air microbubbles[29]. The estimated parameters were then used to predict moles of gas, n_A (N_2 gas) and n_B (O_2 gas) and to predict variation in microbubble radius with time. The physical properties of gases[32, 33] used in calculations are given in Table S2.

4. Results and discussion

4.1 Generating BSA microbubbles: Fig. 1 presents the schematic of experimental setup used for microbubble synthesis. A single T-junction microfluidic device was used which allows cross flow contact of aqueous and gas phases. The aqueous phase consisted of 15 wt% BSA solution and the gaseous phase consisted of Nitrogen (N_2). Microbubbles were formed at the junction of microfluidic channels due to interfacial instabilities caused by viscous and pressure forces. The pressure forces act at the interface due to flow restriction experienced by the liquid stream as the gaseous thread evolves in the outlet channel[34, 35]. The viscous and pressure forces collectively termed as the detaching force, balance the attaching force, surface tension force, acting at the gas-liquid interface during microbubble formation[36, 37]. When the magnitude of the detaching forces equals the magnitude of the attaching force, the gaseous stream splits periodically into a stream of small gas pockets such that each gas pocket is surrounded by two liquid drops resulting into microbubbles. We observed that the microbubble pinch off rate at the junction was directly proportional to the liquid flowrate and inversely proportional to the working gas pressure, similar to other reports[19].

To increase the *in-vitro* stability of microbubbles, freshly prepared microbubbles were subjected to different crosslinking treatments. Fig. 3 presents the schematic of experimental setup used for crosslinking treatments. For non-crosslinked (NC) microbubbles, the microbubbles were collected in DI water at room temperature. For synthesis of thermally crosslinked microbubbles, Fig. 3A, the microbubbles were formed using a single T-junction and collected in hot DI water maintained at 368 ± 2 K. For chemically crosslinked (CC) microbubbles, Fig. 3B, 0.75 % (v/v) glutaraldehyde solution was introduced in the 2nd T-junction connected in series with the 1st T-junction. This allowed BSA microbubbles formed in the 1st T-junction to be contacted with a stream of glutaraldehyde in the second T-junction.

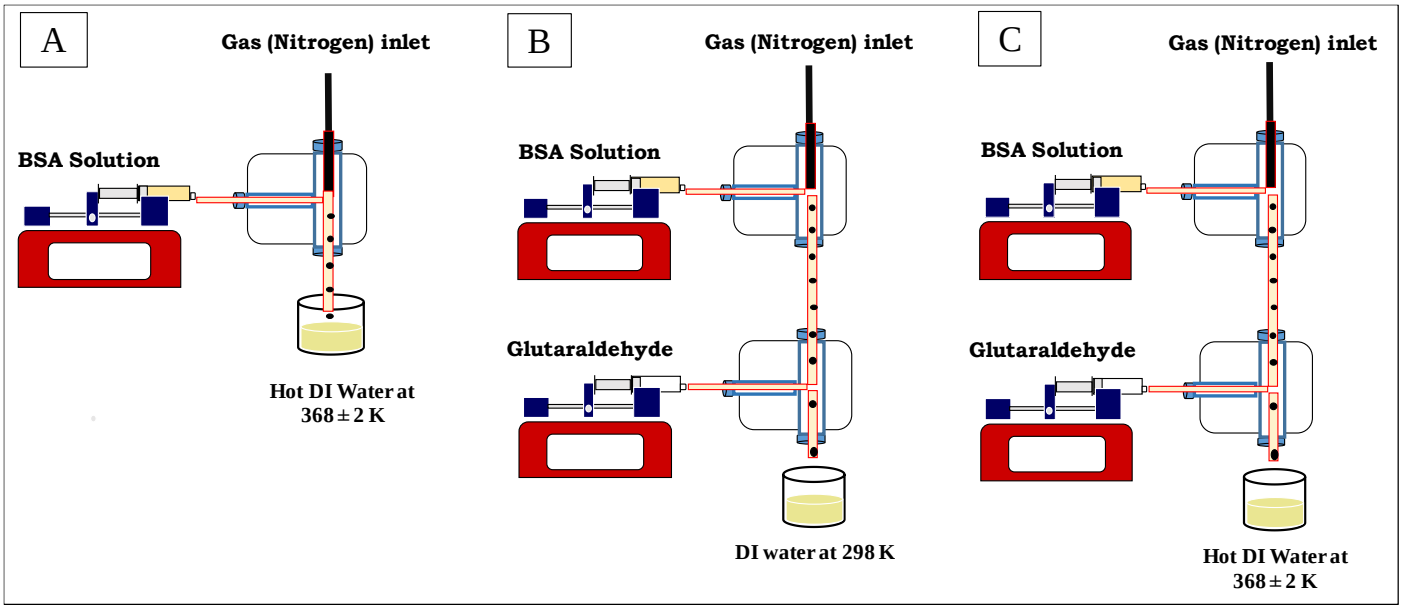

Figure 3: Schematic of experimental setup used for microbubble generation and different crosslinking treatments. (a) For thermal crosslinking (TC), microbubbles are synthesized using a single T-junction and collected in hot water at 368 ± 2 K. (b) For Chemical crosslinking (CC), 0.75% (v/v) Glutaraldehyde was added in the second T-junction and microbubbles were collected in DI water at room temperature. (c) For combined treatment of Thermal and Chemical crosslinking (TC & CC), Glutaraldehyde was added in the second T-junction and microbubbles were collected in hot water at 368±2 K. (CC & TC).

To avoid inter-bubble crosslinking, the microbubbles formed at the T-junction were collected in DI water maintained at room temperature so as to dilute GA solution. To produce microbubbles which are crosslinked by the combined treatment, i.e. chemical as well as thermal crosslinking (CC & TC), Fig. 3C, the microbubbles were formed by connecting two T-junction in series with 0.75 % (v/v) glutaraldehyde solution flowing through the 2nd T-junction and collected in hot DI water maintained at 368 ± 2 K (95 ± 2 °C).

Fig.4 presents the size distribution (Fig. 4A) and optical micrograph (Fig. 4B) of BSA microbubble synthesized at 0.2 ml/min flowrate of BSA solution and 0.2 bar (gauge pressure) gas pressure. Ten optical images comprising of total 100 microbubbles were processed using Image J to estimate the size distribution of the freshly prepared microbubbles. The average size of microbubbles in the sample was estimated to be 270 ± 1.7 µm. A parametric study was conducted to understand the effect of flow parameters on the size of microbubbles. Fig. S2- S5 present the parametric study for microbubble formation in T-junction. For a single T-junction the size of the microbubble was observed to decrease from ~ 320 µm to 240 µm upon increasing the liquid flowrate from 0.05 ml/min to 0.3 ml/ min at constant pressure of 0.2 bar. The production rate of the

microbubble formation was also observed to increase from 160 to 210 bubbles/sec with the increase in liquid flow rate.

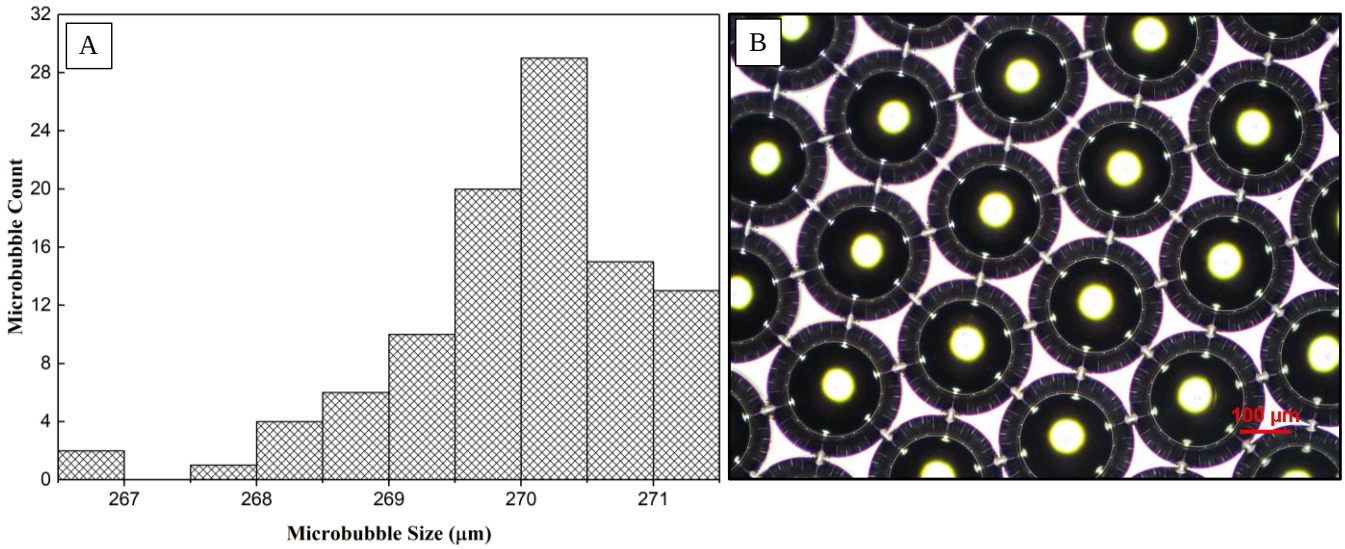

Figure 4: (A) Size distribution (B) Optical micrograph of BSA microbubbles synthesized by at 0.2 ml/min liquid flowrate and 0.2 bar (gauge pressure) gas pressure

On the other hand, the size of microbubble was observed to increase from ~ 290 μm to 340 μm with increase in gas pressure from 0.2 to 0.8 bar gauge pressure at a constant flowrate of 0.1 ml/min and the production rate was observed to decrease from 180 to 160 bubbles/sec. Jiang et.al[11] observed similar trends in variation in size of microbubbles upon variation in flow parameters in a single microfluidic T-junction.

4.2 Estimation of change in % α-helices in microbubble samples subjected to different crosslinking technique: BSA molecules have a tertiary structure composed of α-helices and β-sheets, with 17 intramolecular disulphide bridges and one sulfhydryl group[38]. These intramolecular disulphide bridges provide rigidity to the BSA molecules and also enable modification of BSA molecules upon exposure to different external conditions. Native BSA molecules unfold when denatured and form intermolecular covalent bonds resulting in crosslinking of BSA molecules. In the case of thermal crosslinking, intra molecular di-sulphide bridges in the protein molecules are broken and inter molecular disulphide bonds between the thiol groups of the BSA molecule[1, 38]. In case of chemical crosslinking by glutaraldehyde, covalent bonds are formed between the amino groups of the lysine residue on the BSA surface and the two carbonyl groups of glutaraldehyde[39, 40].

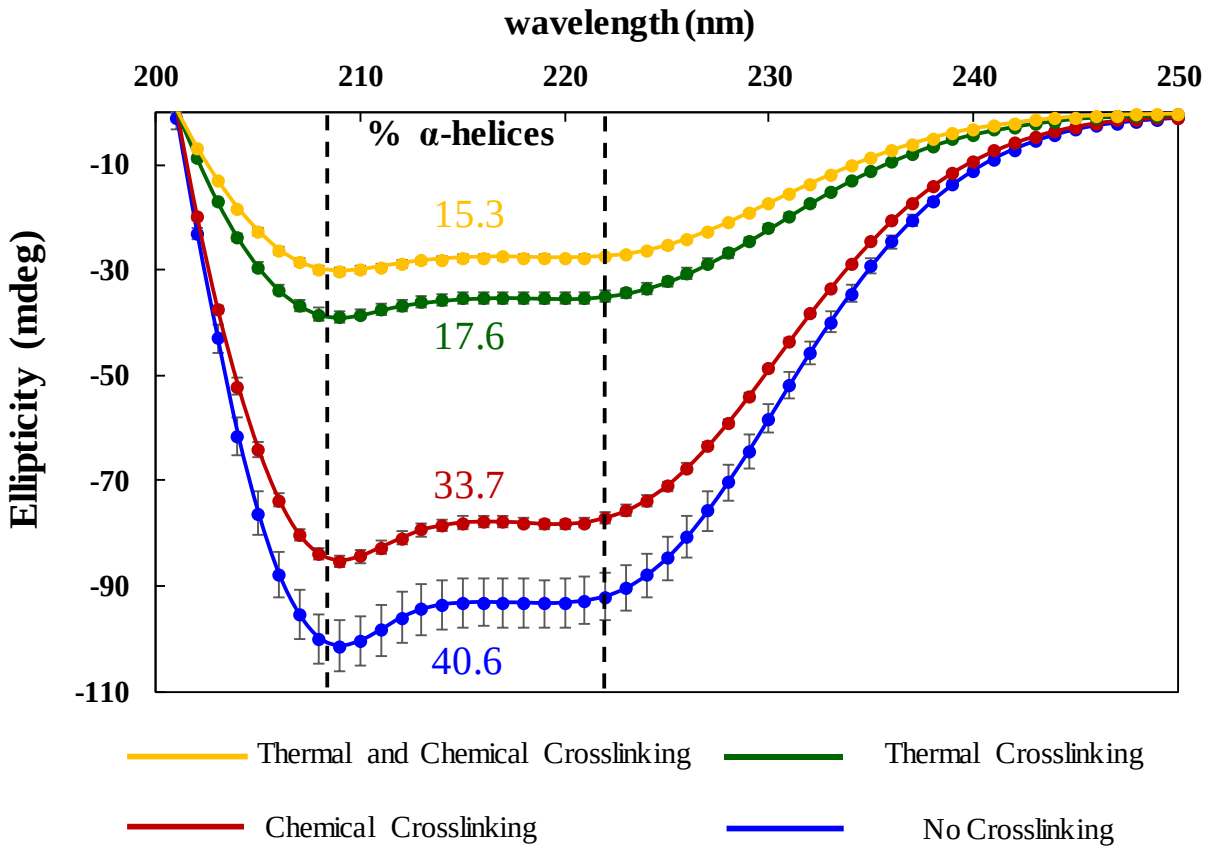

Figure 5: CD spectra of non-crosslinked and crosslinked BSA formulations. % α-helices for BSA formulations are displayed along with the corresponding CD spectra in their respective colour codes

Circular Dichroism (CD) spectroscopy was performed to estimate the conformational changes in the BSA molecules due to different crosslinking treatments. With the help of the CD spectra, % reduction in α-helices of BSA formulations with different treatments were estimated. Fig. 5 presents CD spectra for BSA formulations crosslinked using different treatments such as Chemical Crosslinking only (CC), Thermal Crosslinking only (TC), Thermal and Chemical crosslinking (TC & CC) combined. The Molar ellipticity for BSA formulations were measured in the range of 200 to 250 nm. The estimated values of (%) α-helices are labelled in Fig. 5 and tabulated in Table. S3. BSA is a α–helical protein and consists of a signature negative peak at 208 and 222 nm. The shift in the negative band at these wavelengths reflect changes in the conformation of the BSA molecule. It was observed (Fig. 5) that highest change in the % α-helices was obtained for a combined treatment of thermal and chemical crosslinking. The % α-helices decreased from 40.6 % for BSA solution with no crosslinking to 15.6 % for those with combined chemical and thermal crosslinking (368±2 K) treatment (Fig. 5). Thus, Fig. 5 confirms that the extent of crosslinking obtained by combined treatment of chemical and thermal crosslinking (TC&CC) was higher than chemical crosslinking alone or

thermal crosslinking alone. Interestingly, it can be also observed from Fig. 5 that extent of crosslinking obtained by thermal crosslinking was much higher than chemical crosslinking.

4.3 In-vitro dissolution of Microbubbles in an Air Saturated Aqueous Media: The behaviour of microbubbles in an aqueous environment depends upon the characteristics of their shell and the gas saturation of surrounding aqueous media. The dissolution of microbubbles in an aqueous environment results in the gas exchange phenomena of microbubbles, where microbubbles with different gas core behave differently upon exposure to the aqueous media. Freshly synthesized microbubbles of ~270 μm diameter were observed under optical microscope until complete dissolution. Fig. 6 presents the dissolution profiles for microbubbles subjected to different treatments such as no crosslinking (NC), Chemical Crosslinking (CC) using glutaraldehyde (0.75 % v/v), and Thermal Crosslinking (TC) using hot water (368 ± 2 K) and chemical and thermal crosslinking (TC & CC) combined. Three microbubble dissolution experiments were conducted for each treatment and their corresponding dissolution profiles were plotted along with standard deviation in dissolution time and diameter. Curve with Blue marker in Fig. 6 presents the dissolution profile for ~270 μm N_2 core microbubbles with no crosslinking, dissolving in an air saturated aqueous environment. Fig. 7 (A-D) presents the optical micrographs of different stages of dissolution for non-crosslinked microbubble. It was observed that during microbubble dissolution, non-crosslinked microbubbles did not experience an expansion phase as observed for microbubbles of gases other than air. Reports[29, 33, 41] on albumin and lipid microbubbles show that microbubbles with air as the gas core show only reduction in the size of the whereas SF_6/PFB microbubbles increase initially and then decreases in size during dissolution. The dissolution time for the non-crosslinked microbubbles was found to be 62 (± 4) mins. At the end of dissolution, the microbubble was observed to dissolve completely without leaving any shell, as shown in Fig. 7 C & D. To increase microbubble *in vitro* stability, microbubbles were cross-linked by chemical and thermal treatments to form stable shells. The curves with red, green and pink markers in Fig. 6 represent the dissolution profiles of chemically cross-linked microbubbles, thermally crosslinked microbubbles and microbubbles treated with combination of chemical and thermal crosslinking, respectively. Fig. 7 (E-H), (I-L) and (M-P) present the snapshots of the different stages of microbubble dissolution.

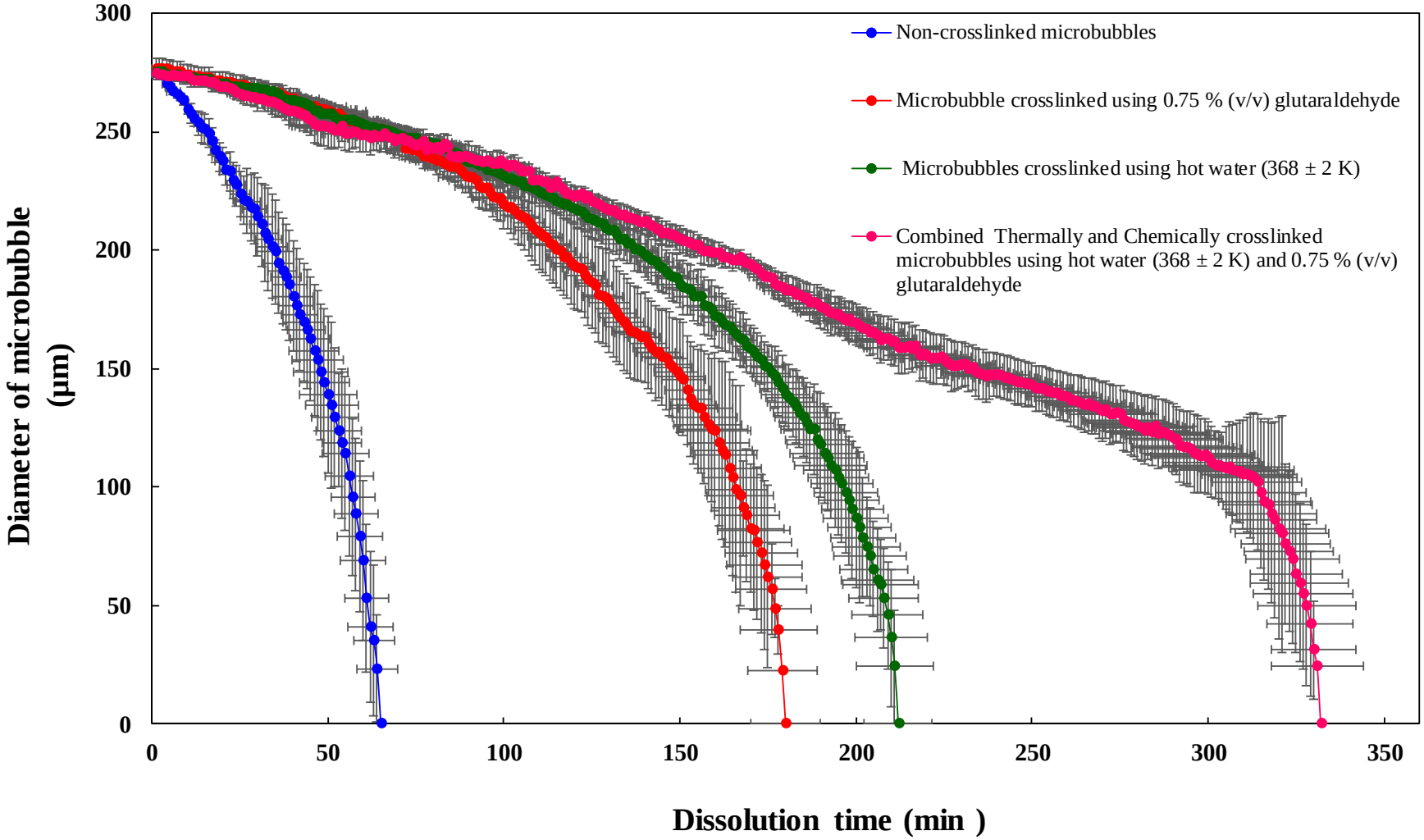

Figure 6: Dissolution profiles of microbubbles dissolving in an air saturated aqueous environment. Blue , Red, Green and Pink markers represent the dissolution profile of Non-Crosslinked microbubbles (NC), Chemically Crosslinked microbubbles (CC), Thermally Crosslinked microbubbles (TC), and Chemically and thermally combined microbubbles (CC and TC), respectively.

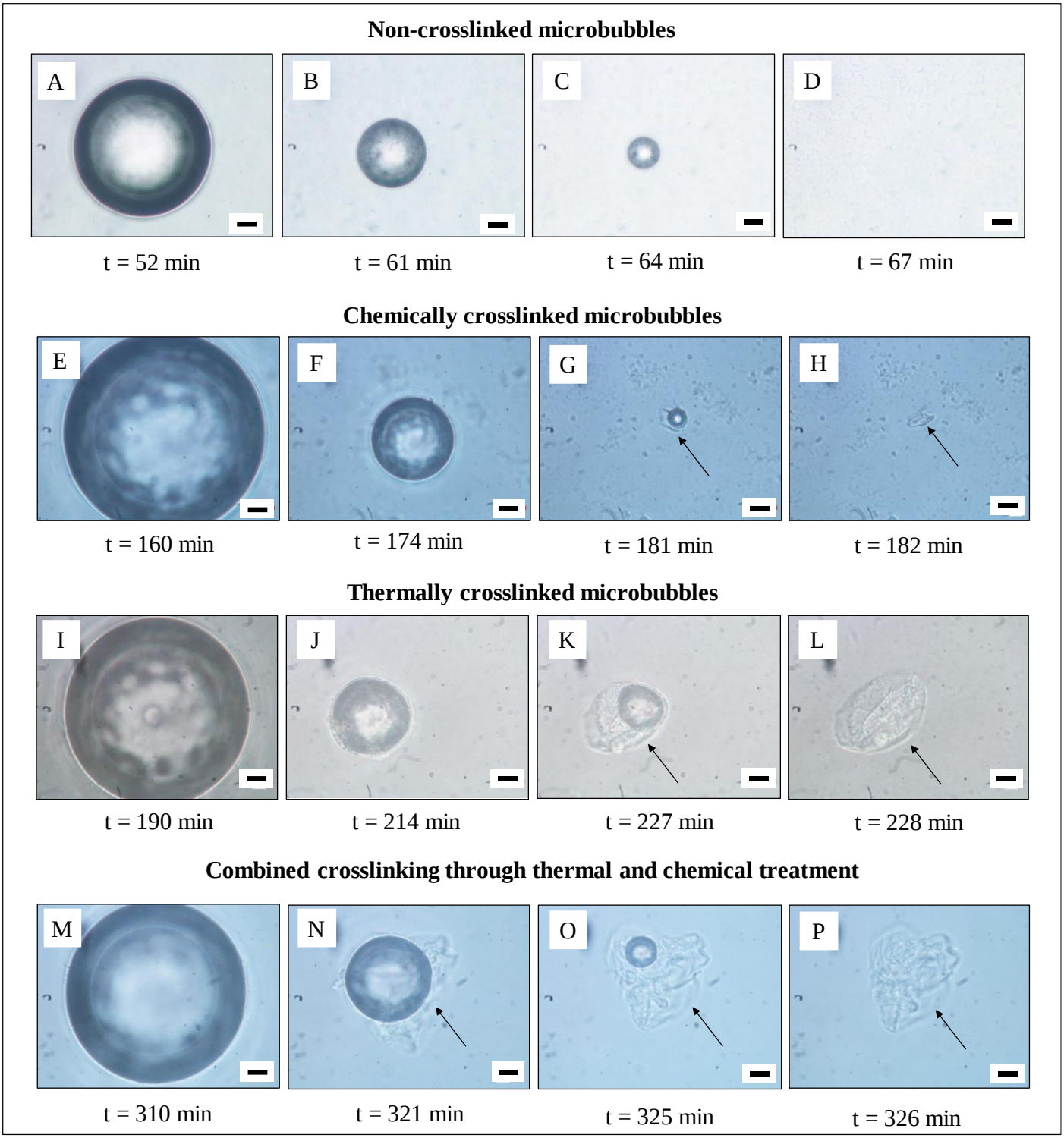

Figure 7: Snapshots of different stages of microbubbles dissolution capturing the shell release form the microbubble surface. (A-D) Non-Crosslinked microbubbles, (E-H) Chemically crosslinked microbubbles, (I-L) Thermally crosslinked microbubbles, (M-P) Combined crosslinking through thermal and chemical treatment. (H, L, P) present the disengaged shell after complete dissolution of the microbubbles. Arrows indicate locations of shell release. Scale bar = 10 µm.

Confocal Microscopy was performed to confirm the detachment of microbubble shell. TC & CC microbubbles stained with Rhodamine b were collected over a glass side with excess water to allow dissolution of

microbubbles. The left-over MB shells were imaged using confocal microscopy. Fig. S6 presents the confocal image of the crumpled MB shell. The dissolution time of all the cross-linked microbubbles was higher as compared to the non-crosslinked microbubbles. It was also observed that the dissolution time of TC & CC treated microbubbles was highest as compared to other crosslinking treatments. The dissolution time of the TC & CC treated microbubbles were 332 ± 12 mins, which was higher than the dissolution times of 179 ± 5 mins and 212 ± 5 mins for the CC microbubbles and TC treated microbubbles, respectively. This suggests that an increase in the extent of crosslinking of microbubble shell reduces diffusion of gas from the core of microbubble to the aqueous environment, which then increases microbubble dissolution time.

It was also observed that cross-linked microbubbles showed a distinct dissolution behaviour compared to the non-crosslinked microbubbles during the final stage of the dissolution. For crosslinked microbubbles it was observed that as the microbubble reduced to a considerable size, a part of shell began to disengage from the microbubble surface and the shell was observed to disengage continuously thereafter during the rest of the dissolution (See S1.mp4, S2.mp4 and S3.mp4). The decrement in microbubble size became faster upon disengagement of the microbubble shell, suggesting that the resistance offered by the microbubble shell for gas diffusion has decreased[29]. After the complete dissolution of the microbubbles a considerable amount of shell was left over as compared to the non-crosslinked microbubbles (See S4.mp4). The extent of shell release was observed to be higher for combined thermal and chemical crosslinking (See S1.mp4) as compared to thermal (See S2.mp4) and chemical crosslinking (See S3.mp4) alone. The dissolution profiles (radius vs time data) of microbubbles were fed to the mass transfer model to estimate the shell resistance of microbubbles and elucidate the gas-exchange phenomena for N_2 microbubbles subjected to different crosslinking treatments.

4.4 Estimation of shell parameters using mass transfer model for microbubble dissolution

In order to understand the effect of different cross-linking methods on the characteristics of microbubbles shell such as shell resistance, microbubble dissolution profiles were analysed using mass transfer model which describes gas-exchange phenomena during microbubble dissolution. Microbubbles dissolution data (Radius v/s Time) was used to estimate the shell resistance values for microbubbles subjected to different crosslinking treatments. Fig. S7 presents experimental dissolution profiles of chemically crosslinked microbubbles and the numerical fits obtained after applying the mathematical model. The numerical fits were perfect with a R^2 value

of 0.98. Similar exercise was performed for microbubbles subjected to other cross-linking treatments and also for non-crosslinked microbubbles. Table 1 presents estimated shell resistances for microbubbles subjected to different cross-linking treatments. Among the different treatments, larger shell resistances for the permeation of N_2 and O_2 gases were obtained for microbubbles subjected to the combined treatment of thermal and chemical crosslinking where the shell resistances were estimated to be 20.4 (± 1.1) × 10^4 sec/m and 46.2 (± 4.2) × 10^4 sec/m for N_2 and O_2 gases, respectively. The higher value of shell resistance for these microbubbles again confirms that a combined chemical and thermal crosslinking treatment results in highly crosslinked shell which increases the permeation resistance for gas transport. For thermally crosslinked microbubbles, the shell resistances were found to be 9.4 (± 2.3) × 10^4 and 22.3 (± 5.5) × 10^4 for N_2 and O_2 gases, respectively, which were observed to be higher than those for chemically crosslinked microbubbles [6.1 (± 2.5) × 10^4 and 13.4 (± 1.13) × 10^4 for N_2 and O_2 gases, respectively] suggesting that microbubbles treated with hot water form a better crosslinked shell as compared to chemically crosslinked shell.

Table 1: Overall mass transfer resistances (estimated using mass transfer model), shell thickness of BSA shells subjected to different crosslinking treatments

Treatment	Resistance for N_2 (sec/m)	Resistance for O_2 (sec/m)	Shell Thickness (nm)
No crosslinking	3.7 (± 0.9)×10^4	6.4 (± 0.95)×10^4	-
Chemical Crosslinking	6.1 (± 2.5)×10^4	13.4 (± 1.13)×10^4	57 (± 11)
Thermal Crosslinking	9.4 (± 2.3)×10^4	22.3 (± 5.5)×10^4	97 (± 18)
Thermal and Chemical crosslinking	20.4 (± 1.1)×10^4	46.2 (± 4.2)×10^4	140 (± 15)

The lower values of the shell resistances (Table 1) and the lower reduction in % alpha-helices of the chemically crosslinked BSA shell (Fig. 5) compared to thermally crosslinked microbubble shells suggest that chemical crosslinking strictly depends upon the exposure of the dilute glutaraldehyde stream and the BSA stream in the

microfluidic devices and since these microbubbles were immediately collected in dilute DI water to avoid inter-bubble crosslinking, the overall concentration of glutaraldehyde decreased drastically and resulted in lower extent of shell crosslinking. The collection of microbubbles in hot water for thermal crosslinking on the other hand directly leads to immediate and better crosslinking. Therefore, it can be observed from Fig. 5 and Table 1 that the extent of denaturation and mass transfer resistances for thermally crosslinked shells were higher than chemically crosslinked shells. The lowest shell resistances for non-crosslinked microbubbles suggests that the non-crosslinked shell was highly preamble for gas transport and provided relatively lower mass transfer resistances during microbubble dissolution compared to crosslinked microbubbles.

4.5 Change in moles, surface tension and shell resistance during microbubble dissolution: Fig. 8A presents changes in moles of gases, Nitrogen (n_A, N_2) and Oxygen (n_B, O_2), and change in total moles of gaseous species ($n_T = n_A + n_B$) for chemically crosslinked N_2 microbubble dissolving in an air-saturated aqueous environment. The simulation results show that moles of nitrogen decrease while the moles of oxygen in the microbubble goes through maximum during microbubble dissolution. Initially, the chemical potential of nitrogen is higher inside the bubble as compared to the outer aqueous environment. Due to the difference in the chemical potential, N_2 diffuses out of the microbubble. Unlike air microbubbles, since the N_2 microbubble core is devoid of oxygen, O_2 gas diffuses into the microbubble when exposed to an air-saturated aqueous medium. Initially, the chemical potential gradient for oxygen is high, but it decreases with time during the dissolution due to the continuous influx of O_2 into microbubble. The simultaneous efflux of N_2 and influx of O_2 during the dissolution slows down the rate of change of microbubbles size during the initial phase of the dissolution process (as can be observed from slope of dissolution curve during the initial dissolution phase). The number of moles of O_2 goes through a maximum, and the number of moles of N_2 decreases continuously. After reaching the maximum, the number of moles of O_2 decreases, reflecting the reversal of the concentration gradient due to higher Laplace pressure inside the bubble[30, 33]. Both N_2 and O_2 now diffuse out of microbubble during the rest of the dissolution process. The dissolution becomes relatively faster upon efflux of gases, highlighted by the change in slope of the dissolution curve. Fig. 8B presents the plot for change in surface tension and shell resistance with time during microbubble dissolution.

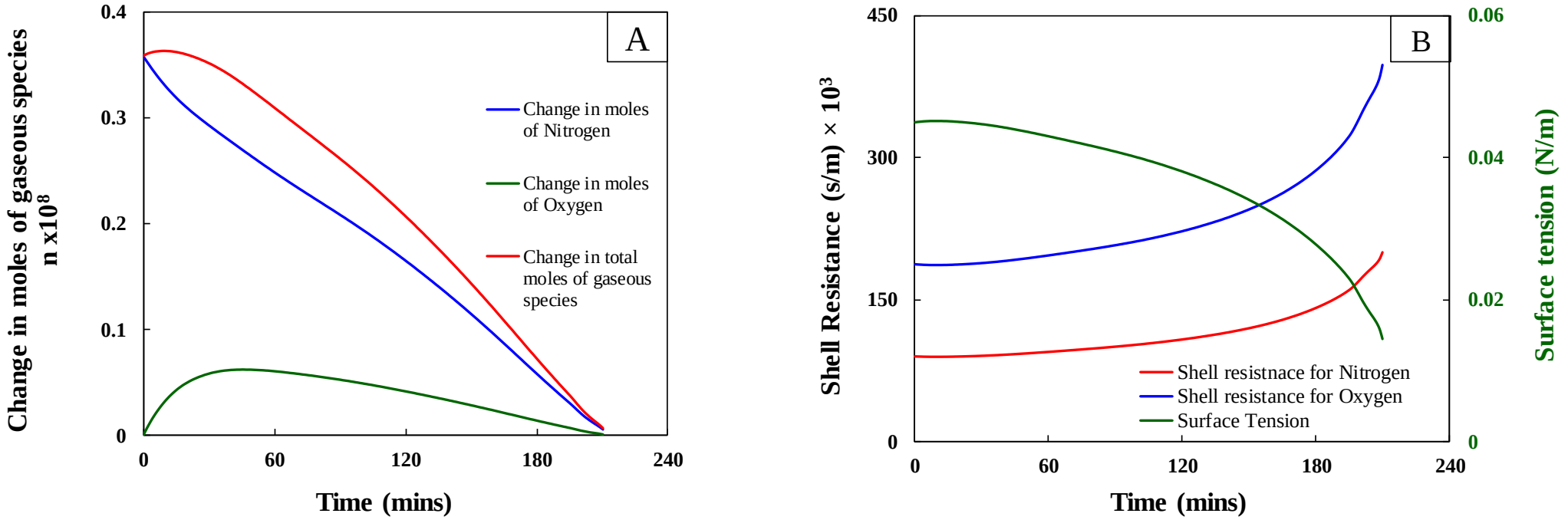

Figure 8: (a) Change in the number of moles of gas species in the microbubble during the dissolution of 270 µm (diameter) N_2 microbubbles subjected to chemical crosslinking, dissolving in an air saturated aqueous medium and (b) Change in surface tension at gas-liquid interface and shell resistances during microbubble dissolution

As the microbubble reduces in size, the surface tension at the gas-liquid interface decreases, and the shell resistance increases. As the microbubble reduces in size during dissolution, the BSA molecules at the interface come closer to each other and as a result, the interaction between BSA molecules increases, and the surface tension decreases. On the other hand, as the molecules come closer to each other, the pores or the microbubbles shell defects decrease and restrict diffusion of gases from the microbubbles core to the air saturated medium, which results in higher mass transfer resistance.

4.6 Surface morphology and topography of microbubble shells obtained post microbubble dissolution

Fig. S8 presents SEM images of MB shells subjected to different crosslinking methods. Non-crosslinked BSA shells dissolved completely during microbubble dissolution, contrary to crosslinked microbubbles. Fig. S8 shows that microbubbles treated to TC, CC and a combination of TC & CC yield ruptured microbubble shells at the end of microbubble dissolution. These collapsed BSA shells are obtained at the end of dissolution mainly due to the crosslinking of BSA molecules. The SEM micrographs of collapsed microbubble shells were processed in MATLAB to estimate the shell thickness. To identify the edges of the microbubble shells, contour maps (Fig. 9) also known as the elevation maps were plotted for SEM micrographs.

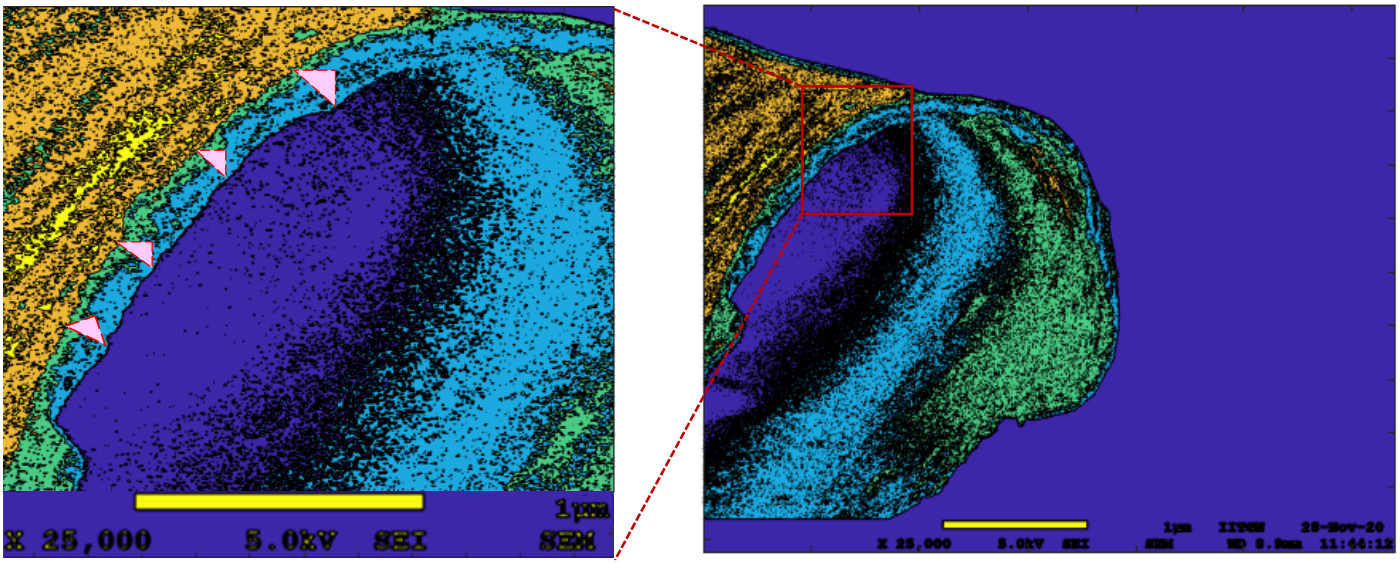

Figure 9: Example of contour map of SEM micrograph at 25000X for estimation of shell thickness.

The contour map, shown in Fig. 9, connects points at equal elevation and colour-codes surfaces at different elevations, enabling identification of a clear edge. The thickness of the BSA shell crosslinked with TC & CC was found out to be 140 (±15) nm. Figs. S9 & S10 present the contour maps for thermal and chemical crosslinked microbubble shells, the shell thicknesses for which were found to be 97 (± 18) nm and 52 (± 11)

nm, respectively. Further, Fig. S11 presents AFM images highlighting the surface topography of crosslinked microbubble shells. Shell roughness values (R_{max}) were estimated to be 6.1, 10.4 and 20.5 nm for CC, TC and combined treatment of TC & CC, respectively, confirming again that combined treatment of TC & CC resulted in higher extent of denaturation and hence better crosslinking of BSA shell and higher shell thickness. Consequently, a thicker shell obtained by the combined treatment of TC & CC provides better in-vitro stability for microbubbles against dissolution by providing higher shell resistances to mass transfer of gases diffusing out of microbubbles.

5. Conclusions: Microfluidic devices such as T-junctions can produce monodisperse microbubbles but these microbubbles have very poor stability in aqueous medium. In this work, we have attempted to enhance *in-vitro* dissolution stability of microbubbles synthesized using microfluidic T-junction devices. Microbubbles were subjected to chemical crosslinking, thermal crosslinking and a combined treatment of chemical and thermal crosslinking. It was observed that microbubbles crosslinked by a combined treatment of thermal and chemical crosslinking persisted longer in an air-saturated aqueous environment as compared to chemical and thermal crosslinking alone. While the dissolution time for non-crosslinked microbubbles was found to be 62 (± 4) min, the dissolution time increased to 332 (± 12) mins for microbubbles subjected to a combined treatment of TC & CC. Interestingly, unlike non-crosslinked microbubbles, *in-vitro* dissolution of cross-linked microbubbles resulted in shell debris at the end of dissolution with higher shell debris found for microbubbles subjected to a combined treatment of TC & CC. The experimental radius v/s time plots were fitted numerically to a mass transfer model to estimate shell resistances. The simulation results showed that microbubble shells crosslinked by a combined treatment of TC & CC imparted higher mass transfer resistances during microbubble dissolution. Contour maps plotted for BSA shells using SEM micrographs and AFM analysis of BSA shells showed that the shell thickness and shell roughness of microbubbles subjected to a combined treatment of TC & CC were highest corroborating CD spectroscopy analysis which confirmed higher BSA denaturation during a combined treatment of TC & CC.

Supporting Information

Physicochemical properties of BSA solution used in this study (Table S1), Physical properties of gases (Table S2), % α-helices estimated from CD spectra for BSA formulations crosslinked using different treatments

(Table S3), Schematic of the experimental setup for dissolution study (Fig. S1), Change in average microbubbles size and production rate upon increase in gas pressure at constant flowrate of BSA solution at 0.1 ml/min (Fig. S2), Microscopic images of microbubbles with the increase in gas pressure from 0.2 bar to 0.8 bar (gas pressure) at a constant liquid flowrate of 0.1 ml/min (Fig. S3), Change in average microbubbles size and production rate upon increase in BSA solution flowrate at constant pressure 0.2 bar (Fig. S4), Microscopic images of microbubbles with increase in liquid flowrate from 0.05 ml/min to 0.3 ml/min at constant gas pressure 0.2 bar (Fig. S5), Confocal Images of crumpled microbubble shell stained with Rhodamine B (Fig. S6), Comparison of the numerical fit and the experimental dissolution data (Fig. S7), SEM micrographs of collapsed microbubble shells subjected to different treatments (Fig. S8), Contour plots of thermally crosslinked alone and chemically crosslinked alone microbubble shell (Figs. S9, and S10), AFM images of microbubble shell for scan 10 × 10 μm^2 area, 2-D scans 3-D scans, for microbubble subjected to different treatments (Fig. S11). Dissolution video of combined thermal and chemical crosslinked microbubble (Video S1.mp4), Dissolution video of thermally crosslinked microbubble (Video S2.mp4), Dissolution video of chemically crosslinked microbubble (Video S3.mp4), Dissolution video of non-crosslinked microbubble (Video S4.mp4).

Acknowledgements: The authors gratefully acknowledge the funding from UGC-UKIERI Joint Research Programme (UKIERI III) through a grant no. 184-7/2018 (IC). The authors acknowledge the mechanical workshop facility at UCL, Central Instrumentation Facility at IITGN to carry out this work. The authors also acknowledge the financial support from Ministry of Education (MoE), Government of India

References

1. Grinstaff, M. W.; Suslick, K. S., Air-filled proteinaceous microbubbles: synthesis of an echo-contrast agent. *Proceedings of the National Academy of Sciences* **1991,** *88* (17), 7708-7710.
2. Upadhyay, A.; Dalvi, S. V., Synthesis, characterization and stability of BSA-encapsulated microbubbles. *RSC Advances* **2016,** *6* (18), 15016-15026.
3. Sirsi, S.; Borden, M., Microbubble Compositions, Properties and Biomedical Applications. *Bubble Sci Eng Technol* **2009,** *1* (1-2), 3-17.
4. Chowdhury, S. M.; Lee, T.; Willmann, J. K., Ultrasound-guided drug delivery in cancer. *Ultrasonography* **2017,** *36* (3), 171.
5. Garbin, V., Dynamics of Coated Microbubbles in Ultrasound. In *The Micro-World Observed by Ultra High-Speed Cameras*, Springer: 2018; pp 357-374.

6. Porter, T. R.; Xie, F.; Kilzer, K., Intravenous perfluoropropane-exposed sonicated dextrose albumin produces myocardial ultrasound contrast that correlates with coronary blood flow. *Journal of the American Society of Echocardiography* **1995,** *8* (5), 710-718.
7. Porter, T. R.; Xie, F.; Kricsfeld, A.; Deligonul, U.; Kilzer, K., Reduction in left ventricular cavitary attenuation and improvement in posterior myocardial contrast with higher molecular weight intravenous perfluorocarbon-exposed sonicated dextrose albumin microbubbles. *Journal of the American Society of Echocardiography* **1996,** *9* (4), 437-441.
8. Upadhyay, A.; Dalvi, S. V., Microbubble formulations: synthesis, stability, modeling and biomedical applications. *Ultrasound in medicine & biology* **2019,** *45* (2), 301-343.
9. Parhizkar, M.; Stride, E.; Edirisinghe, M., Preparation of monodisperse microbubbles using an integrated embedded capillary T-junction with electrohydrodynamic focusing. *Lab on a Chip* **2014,** *14* (14), 2437-2446.
10. Farook, U.; Stride, E.; Edirisinghe, M.; Moaleji, R., Microbubbling by co-axial electrohydrodynamic atomization. *Medical & biological engineering & computing* **2007,** *45* (8), 781-789.
11. Jiang, X.; Zhang, Y.; Edirisinghe, M.; Parhizkar, M., Combining microfluidic devices with coarse capillaries to reduce the size of monodisperse microbubbles. *RSC advances* **2016,** *6* (68), 63568-63577.
12. Parhizkar, M.; Edirisinghe, M.; Stride, E., The effect of surfactant type and concentration on the size and stability of microbubbles produced in a capillary embedded T-junction device. *Rsc Advances* **2015,** *5* (14), 10751-10762.
13. Mahalingam, S.; Raimi-Abraham, B. T.; Craig, D. Q.; Edirisinghe, M., Formation of protein and protein–gold nanoparticle stabilized microbubbles by pressurized gyration. *Langmuir* **2015,** *31* (2), 659-666.
14. Nakata, M.; Tanimura, N.; Koyama, D.; Krafft, M. P., Adsorption and Desorption of a Phospholipid from Single Microbubbles under Pulsed Ultrasound Irradiation for Ultrasound-Triggered Drug Delivery. *Langmuir* **2019,** *35* (31), 10007-10013.
15. Kopechek, J. A.; McTiernan, C. F.; Chen, X.; Zhu, J.; Mburu, M.; Feroze, R.; Whitehurst, D. A.; Lavery, L.; Cyriac, J.; Villanueva, F. S., Ultrasound and microbubble-targeted delivery of a microRNA inhibitor to the heart suppresses cardiac hypertrophy and preserves cardiac function. *Theranostics* **2019,** *9* (23), 7088.
16. Sun, Y.; Luo, J.; Chen, J.; Xu, F.; Ding, X.; Huang, P., Ultrasound-mediated microbubbles destruction for treatment of rabbit VX2 orthotopic hepatic tumors. *Applied Acoustics* **2018,** *138*, 216-225.
17. Zhang, H.; Peng, Y.-L.; Wang, H.; Huang, J.-B.; Yan, F., Preparation of VEGFR2 Targeted Ultrasound Microbubbles by Freeze-drying and Targeting Study in vitro. *Sichuan da xue xue bao. Yi xue ban= Journal of Sichuan University. Medical Science Edition* **2018,** *49* (6), 955-959.
18. Feshitan, J. A.; Chen, C. C.; Kwan, J. J.; Borden, M. A., Microbubble size isolation by differential centrifugation. *Journal of Colloid and Interface Science* **2009,** *329* (2), 316-324.
19. Parhizkar, M.; Edirisinghe, M.; Stride, E., Effect of operating conditions and liquid physical properties on the size of monodisperse microbubbles produced in a capillary embedded T-junction device. *Microfluidics and nanofluidics* **2013,** *14* (5), 797-808.
20. Fu, T.; Ma, Y.; Funfschilling, D.; Li, H. Z., Bubble formation and breakup mechanism in a microfluidic flow-focusing device. *Chemical Engineering Science* **2009,** *64* (10), 2392-2400.
21. Castro-Hernández, E.; Van Hoeve, W.; Lohse, D.; Gordillo, J. M., Microbubble generation in a co-flow device operated in a new regime. *Lab on a Chip* **2011,** *11* (12), 2023-2029.
22. Kothandaraman, A.; Alfadhl, Y.; Qureshi, M.; Edirisinghe, M.; Ventikos, Y., Effect of the Mixing Region Geometry and Collector Distance on Microbubble Formation in a Microfluidic Device Coupled with ac-dc Electric Fields. *Langmuir* **2019,** *35* (31), 10052-10060.
23. Pancholi, K.; Stride, E.; Edirisinghe, M., Dynamics of bubble formation in highly viscous liquids. *Langmuir* **2008,** *24* (8), 4388-4393.
24. Xu, J.; Li, S.; Chen, G.; Luo, G., Formation of monodisperse microbubbles in a microfluidic device. *AIChE journal* **2006,** *52* (6), 2254-2259.
25. Pulsipher, K. W.; Hammer, D. A.; Lee, D.; Sehgal, C. M., Engineering theranostic microbubbles using microfluidics for ultrasound imaging and therapy: a review. *Ultrasound in medicine & biology* **2018,** *44* (12), 2441-2460.
26. Xu, J.; Li, S.; Wang, Y.; Luo, G., Controllable gas-liquid phase flow patterns and monodisperse microbubbles in a microfluidic T-junction device. *Applied Physics Letters* **2006,** *88* (13), 133506.
27. Fu, T.; Ma, Y.; Funfschilling, D.; Zhu, C.; Li, H. Z., Squeezing-to-dripping transition for bubble formation in a microfluidic T-junction. *Chemical engineering science* **2010,** *65* (12), 3739-3748.
28. Khan, A. H.; Jiang, X.; Surwase, S.; Gultekinoglu, M.; Bayram, C.; Sathisaran, I.; Bhatia, D.; Ahmed, J.; Wu, B.; Ulubayram, K., Effectiveness of oil-layered albumin microbubbles produced using microfluidic T-junctions in series for in vitro inhibition of tumor cells. *Langmuir* **2020,** *36* (39), 11429-11441.

29. Khan, A.; Dalvi, S., Kinetics of Albumin Microbubble Dissolution in Aqueous Medium. *Soft Matter* **2020,** *16*, 2149-2163.
30. Dalvi, S. V.; Joshi, J. R., Modeling of microbubble dissolution in aqueous medium. *Journal of colloid and interface science* **2015,** *437*, 259-269.
31. Blank, M., An approach to a theory of monolayer permeation by gases. *The Journal of Physical Chemistry* **1964,** *68* (10), 2793-2800.
32. Sarkar, K.; Katiyar, A.; Jain, P., Growth and dissolution of an encapsulated contrast microbubble: effects of encapsulation permeability. *Ultrasound in medicine & biology* **2009,** *35* (8), 1385-1396.
33. Kwan, J. J.; Borden, M. A., Microbubble dissolution in a multigas environment. *Langmuir* **2010,** *26* (9), 6542-6548.
34. Garstecki, P.; Fuerstman, M. J.; Stone, H. A.; Whitesides, G. M., Formation of droplets and bubbles in a microfluidic T-junction—scaling and mechanism of break-up. *Lab on a Chip* **2006,** *6* (3), 437-446.
35. De Menech, M.; Garstecki, P.; Jousse, F.; Stone, H. A., Transition from squeezing to dripping in a microfluidic T-shaped junction. *journal of fluid mechanics* **2008,** *595*, 141-161.
36. Sun, L.; Fan, M.; Li, P.; Yu, H.; Zhang, Y.; Xu, J.; Jiang, W.; Qian, S.; Sun, G., Microbubble characteristic in a T-junction microchannel in microfluidic chip. *Molecular Physics* **2019,** *117* (18), 2535-2545.
37. Van Hoeve, W.; Dollet, B.; Versluis, M.; Lohse, D., Microbubble formation and pinch-off scaling exponent in flow-focusing devices. *Physics of fluids* **2011,** *23* (9), 092001.
38. Borzova, V. A.; Markossian, K. A.; Chebotareva, N. A.; Kleymenov, S. Y.; Poliansky, N. B.; Muranov, K. O.; Stein-Margolina, V. A.; Shubin, V. V.; Markov, D. I.; Kurganov, B. I., Kinetics of thermal denaturation and aggregation of bovine serum albumin. *PLoS One* **2016,** *11* (4), e0153495.
39. Habeeb, A.; Hiramoto, R., Reaction of proteins with glutaraldehyde. *Archives of biochemistry and biophysics* **1968,** *126* (1), 16-26.
40. Hopwood, D.; Allen, C.; McCabe, M., The reactions between glutaraldehyde and various proteins. An investigation of their kinetics. *The Histochemical Journal* **1970,** *2* (2), 137-150.
41. Borden, M. A.; Longo, M. L., Dissolution behavior of lipid monolayer-coated, air-filled microbubbles: Effect of lipid hydrophobic chain length. *Langmuir* **2002,** *18* (24), 9225-9233.

TOC Graphic

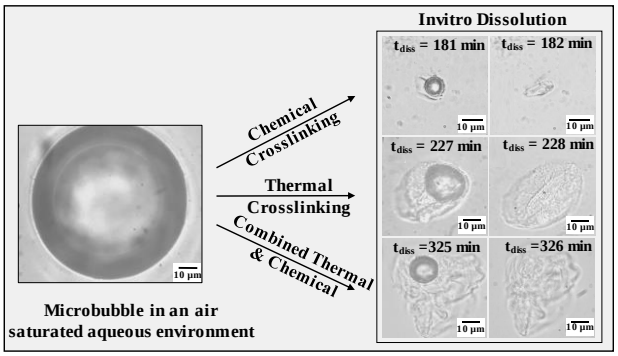
Invitro Dissolution
t_{diss} = 181 min
t_{diss} = 182 min
t_{diss} = 227 min
t_{diss} = 228 min
t_{diss} =325 min
t_{diss} =326 min
10 µm
Chemical Crosslinking
Thermal Crosslinking
Combined Thermal & Chemical
Microbubble in an air saturated aqueous environment

Electronic Supplementary Information

Enhancing Poor In-vitro Dissolution Stability of Albumin Microbubbles produced using Microfluidics T-junction Device

Aaqib H. Khan[#], Swarupkumar Surwase[#], Xinyue Jiang†, Mohan Edirisinghe†, and Sameer V. Dalvi[#]*

Chemical Engineering, Indian Institute of Technology Gandhinagar, Palaj, Gandhinagar - 382355, Gujarat, India

†Department of Mechanical Engineering, University College London (UCL), London WC1E 7JE, U.K.

No. of pages: 8

Table: 3 (S1, S2, S3)

No. of figures: 10 (S4, S5, S6, S7, S8, S9, S10, S11, S12, S13, S14)

Table S1. Physicochemical properties of BSA solution used in this study all measurements were done at room temperature (~25°C)

Aqueous solution	Density (kg/m^3)	Viscosity (mPa s)	Surface tension (mN/m)
15 wt.% BSA	1050 ± 8	1.6 ± 0.25	53 ± 2.7

Table S2. Physical properties of gases

Gases	Molar Diffusivity (m^2/s)	Ostwald Coefficient	Collision Diameter (Å)
N_2	2.20×10^{-9}	1.448×10^{-2}	3.7
O_2	2.01×10^{-9}	2.773×10^{-2}	3.6

Table S3. % α-helices estimated from CD spectra for BSA formulations crosslinked using different treatments

Solution	% α-helices
No Crosslinking	40.6
Chemical crosslinking (CC) using glutaraldehyde solution (0.75 % v/v)	33.7
Thermal crosslinking (TC) using hot water (T = 368 ± 2 K)	17.6
TC & CC combined, glutaraldehyde solution (0.75 % v/v) and hot water (T = 368 ± 2 K)	15.3

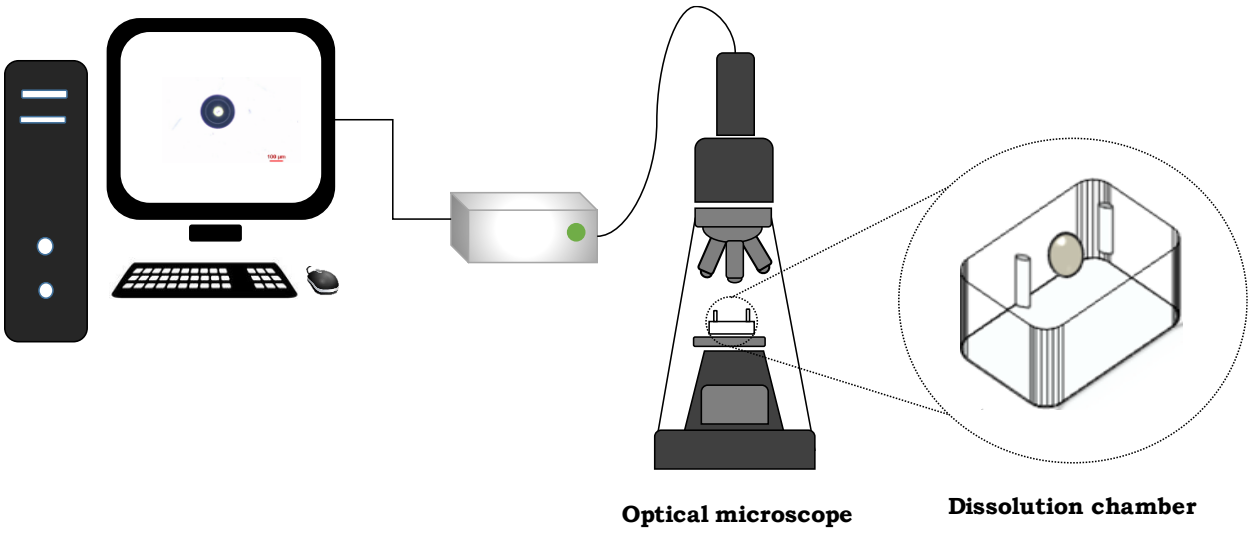

Figure S1. Schematic of the experimental setup for dissolution study

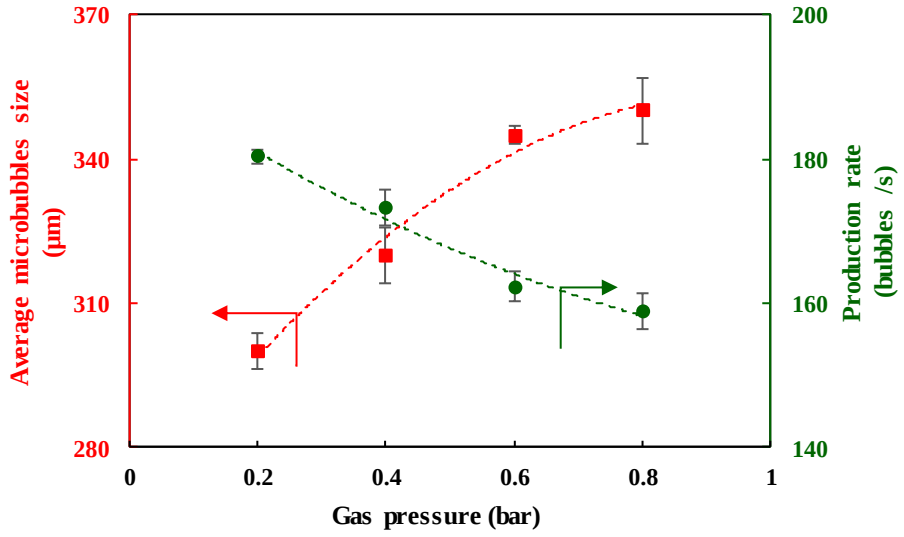

Figure S2. Variation of average microbubbles size with gas pressure at constant flowrate of BSA solution at 0.1 ml/min

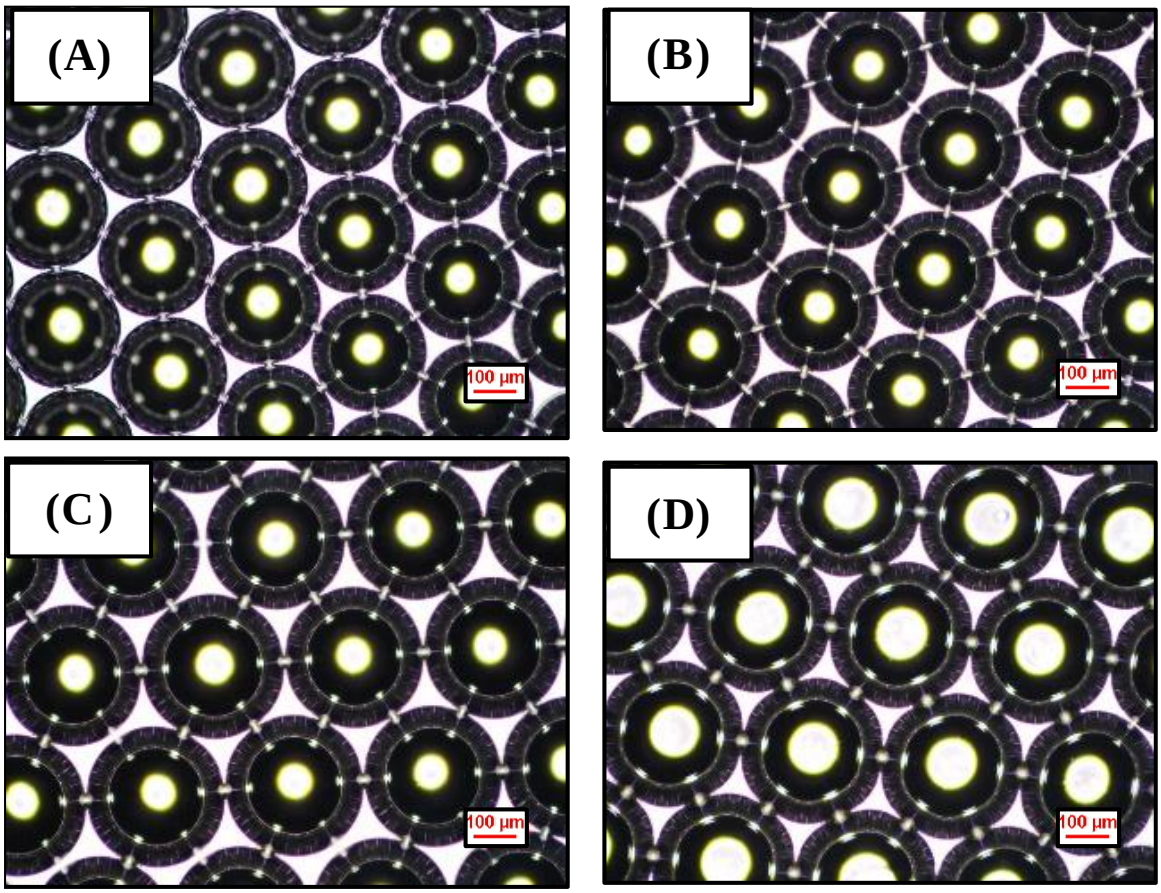

Figure S3. Microscopic images of microbubbles at various gas pressure (A) 0.2 bar (B) 0.4 bar (C) 0.6 bar (D) 0.8 bar

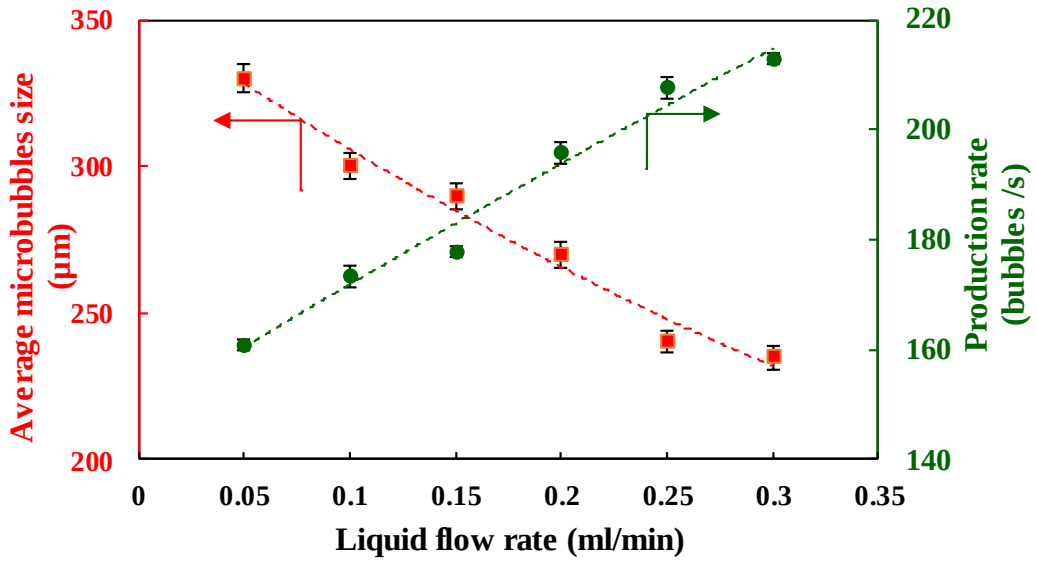

Figure S4. Variation in average microbubbles size with flowrate of BSA solution at constant pressure 0.2 bar

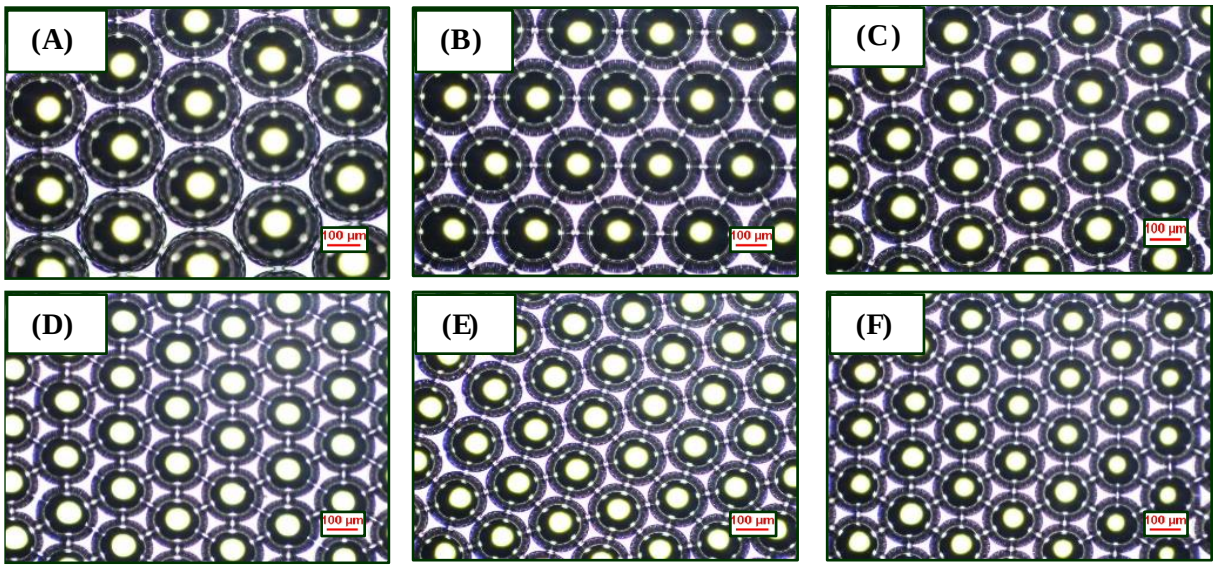

Figure S5. Microscopic images of microbubbles at different liquid flowrate (A) 0.05 ml/min (B) 0.1 ml/min (C) 0.15 ml/min (D) 0.2 ml/min (E) 0.25 ml/min (F) 0.3 ml/min

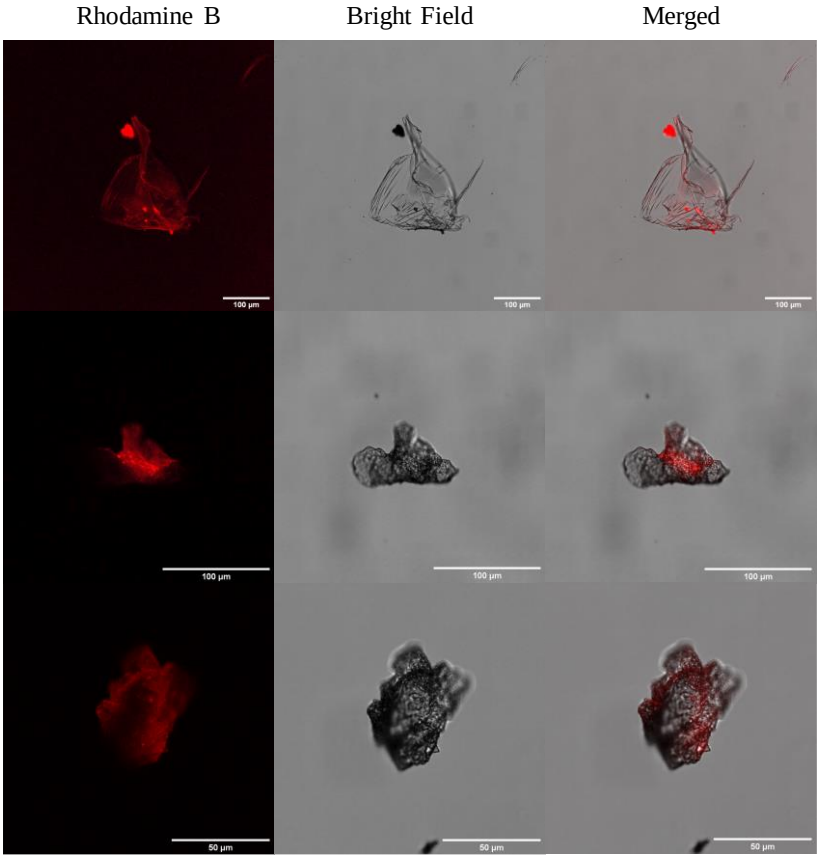

Figure S6. Confocal Images of crumpled microbubble shell. Microbubble shell was stained with Rhodamine B.

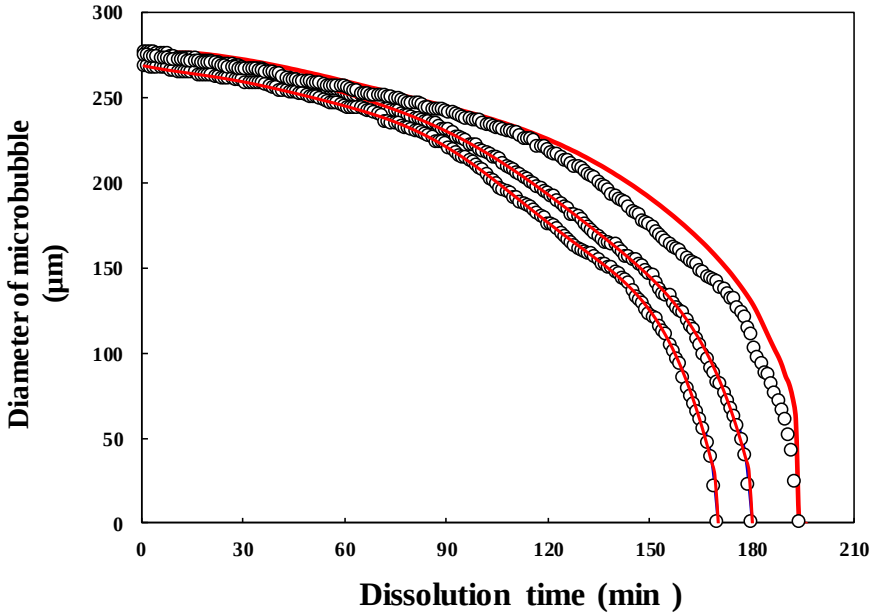

Figure S7. Comparison of the numerical fit and the experimental dissolution data for chemically crosslinked microbubbles dissolving in an air saturated environment

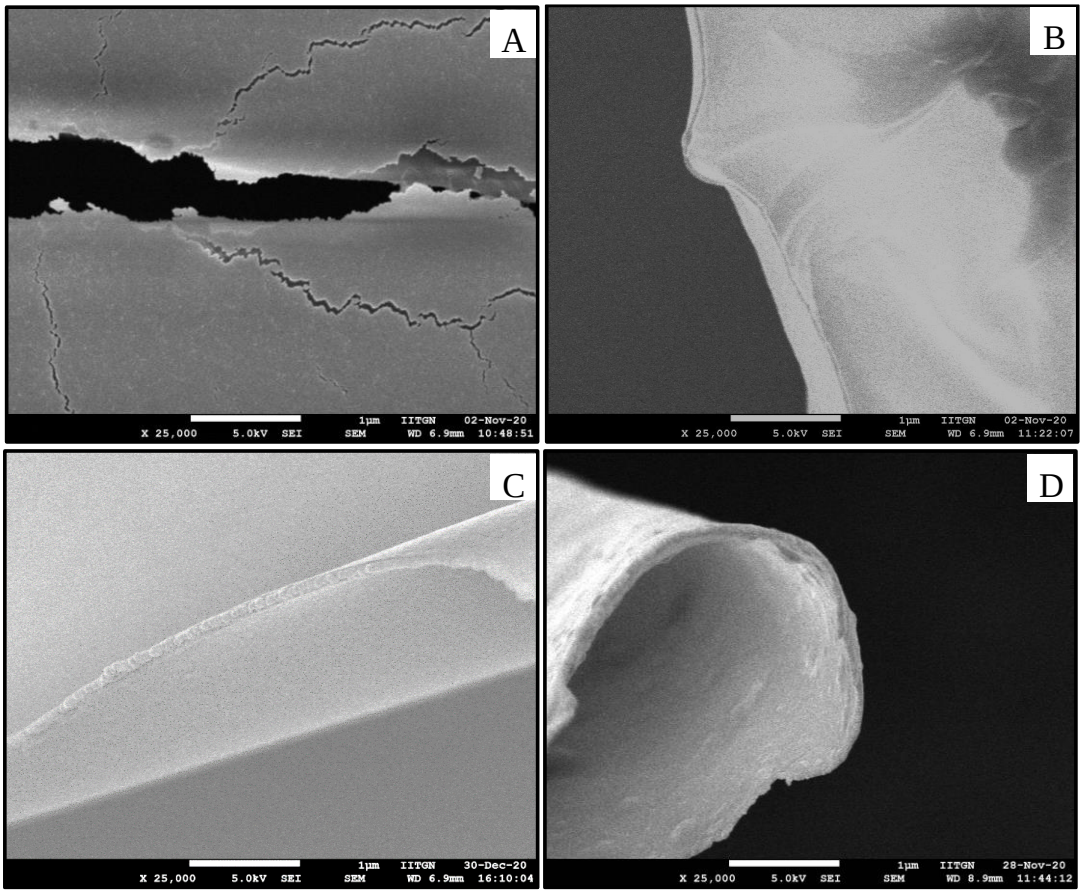

Figure S8. SEM micrographs of collapsed microbubble shells (A) Non-Cross-linked (B) Chemically crosslinked (C) Thermally Crosslinked (D) Combined Thermally and Chemically Crosslinked

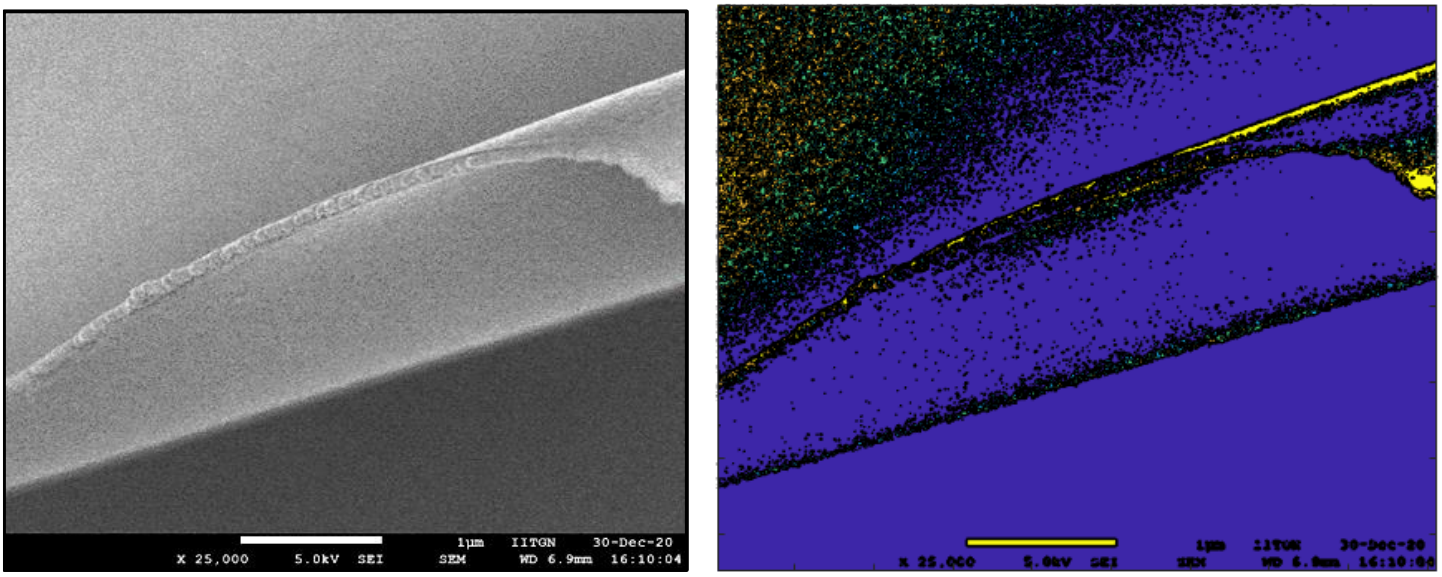

Figure S9. SEM micrograph of thermally crosslinked microbubble shell (left) and contour plot (right)

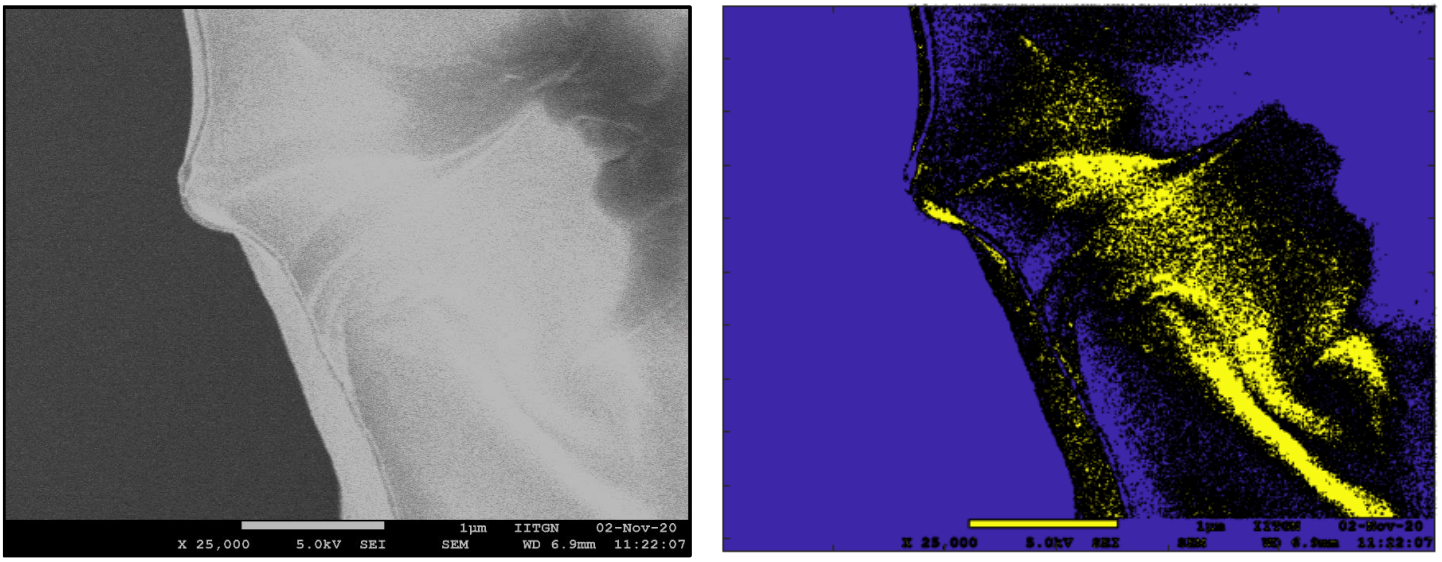

Figure S10. SEM micrograph of chemically crosslinked microbubble shell (left) and contour plot (right)

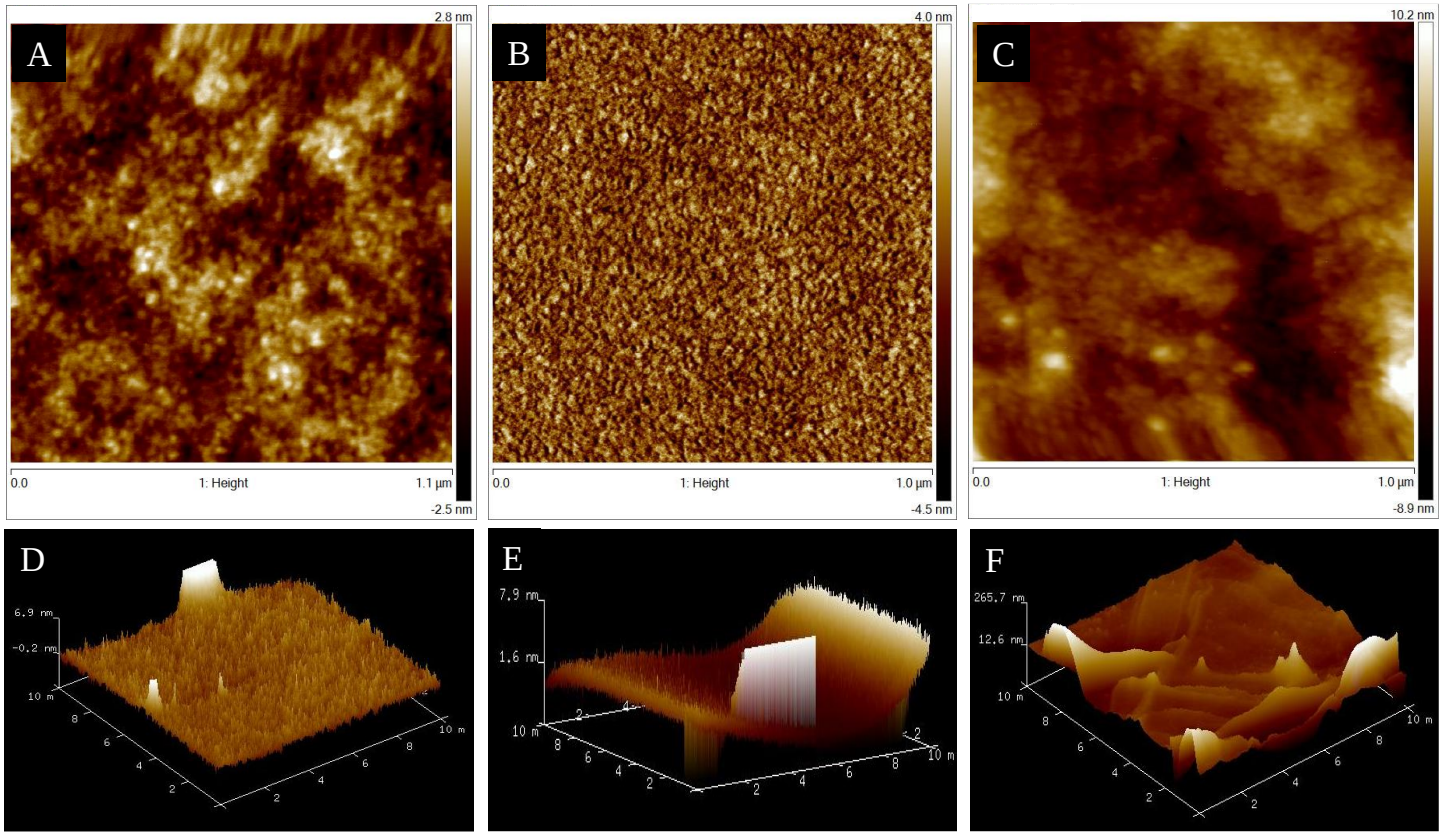

Figure S11. AFM images of microbubble shell for scan area 10 × 10 µm^2 (A-C) 2-D scans and (D-F) 3-D scans for microbubble subjected to (A & D) chemical, (B & E) thermal and (C & F) chemical and thermal combined, respectively.